Bubbles in a Hele–Shaw cell: Numerical simulation of three-dimensional effects

E. Meiburg
Center for Fluid Mechanics, Division of Applied Mathematics, Brown University, Providence, Rhode Island 02912

(Received 15 November 1988; accepted 7 March 1989)

Time-dependent numerical simulations of immiscible bubbles propagating in a Hele–Shaw cell are presented. Purely two-dimensional calculations only show elongated bubbles propagating faster than the viscous fluid, in agreement with Tanveer's results. For small capillary numbers, these bubbles assume circular shapes while their velocity approaches a plateau. By including the leading-order three-dimensional effects on the pressure jump across the interface, wider and shorter bubbles migrating at smaller velocities can be observed. In particular, flattened bubbles and bubbles slower than the viscous phase are found. Even though these bubbles also approach circular shapes for high surface tension values, a velocity plateau is not observed. While noticing that the three-dimensional effects promote a tip instability, the multiple shapes and transitioins observed experimentally can only be partially explained.

I. INTRODUCTION

Immiscible two-phase flows in Hele–Shaw cells (Fig. 1) give rise to a variety of phenomena that are fascinating from a theoretical as well as from an experimental point of view. Viscous fingering, generated by displacing a more viscous fluid in a gap between two flat plates by a less viscous one, has been the traditional focus of numerous papers. Reviews of the literature can be found by Homsy[1] and Saffman.[2] More recently, the flow of bubbles in Hele–Shaw cells has emerged as a similarly interesting problem, in terms of both its stability characteristics[3] and the multitude of shapes found theoretically[4,5] and experimentally.[6] If b denotes the gap width between two flat plates of lateral extent $2L$, it is well known that for small ratios of $\epsilon = b/L$, the equations for the conservation of mass and momentum, formulated in terms of the depth-averaged velocity u and pressure p within each of the two phases, reduce to

$$\nabla \cdot \mathbf{u} = 0 , \tag{1}$$

$$\nabla p = -12\mu \mathbf{u}/b^2 . \tag{2}$$

Appropriate boundary conditions for the interface between the two phases were first formulated by Bretherton[7] and have only recently been discussed in detail by Park and Homsy,[8] as well as by Reinelt,[9] for the case in which the viscous phase wets the wall. They show the difference in the pressure and the normal velocity across the interface to be of the form

$$[p] = (2\sigma/b)(1 + \beta\, \mathrm{Ca}_n^{2/3} + \cdots) + (\sigma/R)[\pi/4 + O(\mathrm{Ca}_n^{2/3})] , \tag{3}$$

$$[\mathbf{n} \cdot \mathbf{u}] = O(\mathrm{Ca}_n^{2/3}) , \tag{4}$$

where σ denotes the surface tension and R the local radius of curvature of the depth-averaged interface position. Here $\mathrm{Ca}_n = U_n \mu/\sigma$ refers to the local capillary number formed with the normal velocity component U_n, the viscosity of the viscous phase μ, and the surface tension σ, as opposed to Ca, which is formed with the velocity far upstream and downstream of the bubble instead of U_n. In addition, β denotes a numerical constant that takes the values of 3.8 and -1.13 for advancing and receding menisci, respectively,[10] if the bubble has equal curvature at the front and rear stagnation points. The factor of $\pi/4$, resulting from the detailed analysis, is different from the factor of 1 used in most two-dimensional calculations.[3–5] However, it can easily be incorporated in the dimensionless parameter governing these two-dimensional calculations without changing the results. For $\mathrm{Ca}_n = 0$ these equations reduce to the Hele–Shaw equations. The above results were obtained by means of a double expansion in ϵ and Ca_n, hence these dimensionless numbers are required to be small. While the first term on the right-hand side of Eq. (3) represents a constant and can consequently be neglected without loss of generality (only pressure gradients are dynamically significant), the second term results in the additional requirement $\epsilon^{-1}\, \mathrm{Ca}_n^{2/3} \ll 1$.

While it is well known that, on the basis of the purely two-dimensional equations and in the absence of side walls, a Hele–Shaw bubble has a circular shape and moves with twice the velocity of the viscous fluid, the motion of a bubble in a cell of finite size has quite different features. The ratio of undisturbed bubble diameter $2a$ to cell width $2L$ now enters into the problem as a further dimensionless number. Taylor and Saffman[11] showed that for the case of zero surface tension there exists a two-parameter family of solutions which, over some range, allows for bubbles of all sizes to move with all velocities, the shape being a function of bubble size and speed. Tanveer[4] recently showed that this degeneracy is removed by introducing surface tension into the two-dimensional problem, with the result that only certain discrete bubble velocities are allowed once the bubble size and surface tension are specified. In this way only certain branches of solutions are possible, termed, by Tanveer, the main branch and the extraordinary branch. The main branch only allows for elongated bubbles propagating faster than the fluid but at less than twice the fluid velocity, and in the limit of large bubbles, it corresponds to the solution found by McLean and Saffman[12] for steady fingers. The most striking feature of the extraordinary branch is the fact that it allows for bubbles with negative curvature at the advancing meniscus. Two further branches were subsequently found by Tan-

 0899-8213/89/060938-09$01.90

veer[5] and called the Romero–Vanden-Broeck branches, since in the limit of large bubble sizes they correspond to solution branches for steady fingers found by those authors.[13,14] These solutions also allow for negative curvature of the advancing meniscus. All of the above steady-state solutions showed bubble velocities larger than the velocity of the surrounding fluid. Tanveer and Saffman[3] examined the linear stability of the various steady-state solution branches. They found that both circular bubbles (no effect of the side walls) and the main branch are linearly stable for nonzero values of the surface tension. The Romero–Vanden-Broeck branches, however, are linearly unstable, with respect to both symmetric and unsymmetric disturbances of the bubble tip. The extraordinary branch found originally by Tanveer[4] is not related to any of the Romero–Vanden-Broeck branches but it is also unstable.[15]

In the light of these findings it comes as a surprise that Kopf-Sill and Homsy[16] experimentally observe six different classes of steady bubble shapes, among them some with short and long tails and others with negative curvature at the leading edge and a shape resembling those of the extraordinary branch found by Tanveer.[4] However, these experimentally observed steady bubble shapes (called "Tanveer" bubbles by Kopf-Sill and Homsy) move at velocities as low as about two-tenths of the velocity of the surrounding fluid, whereas Tanveer's solution had yielded velocities larger than that of the surrounding fluid. Furthermore, the experiments indicate the existence of multiple steady states for the same value of surface tension and bubble size as well as hysteresis effects, as the dimensionless surface tension is varied. In addition, Kopf-Sill and Homsy observe that the bubble shapes cannot be classified on the basis of Ca, $\mathrm{Ca}(a/b)^2$, or $\mathrm{Ca}(a/L)^2$, as would have to be expected from the Hele–Shaw equations. These observations suggest that three-dimensional effects, which are not contained in the two-dimensional equations considered by Tanveer and Saffman,[3] might be of importance in the experiments.

The objective of the current work then is to investigate to what extent three-dimensional effects can explain aspects of the experimentally observed bubble shapes and velocities. From the perturbation analysis mentioned above, we know that the presence of a wetting film of viscous fluid on the flat plates has two main effects: first of all, it causes some "leakage" of the viscous fluid through the thin film, as expressed by the $O(\mathrm{Ca}_n^{2/3})$ term in Eq. (4). However, this leakage should always have the effect of speeding the bubble up,[17] as it now has to displace the same amount of fluid over a smaller area. Since Kopf-Sill and Homsy find bubbles proceeding at velocities much smaller than the values obtained from two-dimensional analysis, the leakage effect of the thin film does not seem to be able to provide an explanation of the experimental observations. A further, more mathematical reason for neglecting the leakage will be given below and is based on the scaled equations.

The second main effect of the thin film concerns the pressure jump across the interface, as reflected in the term $\beta\ \mathrm{Ca}_n^{2/3}$ of Eq. (3). As a result of the presence of the thin film, the radius of curvature of the interface in the thin direction is reduced, thereby increasing the pressure jump. Thus the variation of the film thickness along the interface modifies the pressure gradient within the viscous phase and consequently the forces it exerts on the bubble, resulting in a modificiation of the bubble shape as well as its velocity. Our goal is to assess these effects of the thin film and to study their relevance with respect to the experimental observations by Kopf-Sill and Homsy using Lagrangian numerical simulations. While the calculations are carried out in a two-dimensional fashion, they take into account the leading-order, three-dimensional effects of the thin film on the pressure jump across the interface, according to Eq. (3). We will show that in this way we achieve a better understanding of some of the phenomena observed experimentally by Kopf-Sill and Homsy, i.e., the discrepancy of the measured bubble propagation velocity from the value predicted by two-dimensional theory as well as the variety of steady shapes of bubbles. The comparison between our numerical results and the experiments will have to be of qualitative nature, however, since Eq. (3) is valid only when $\epsilon^{-1}\ \mathrm{Ca}_n^{2/3} \ll 1$. In the experiments of Kopf-Sill and Homsy, ϵ had the value of 130^{-1} while Ca varied from 6×10^{-5}–3×10^{-2}. Thus $\epsilon^{-1}\ \mathrm{Ca}_n^{2/3}$ covers the range from 0.2–12, and hence the majority of experiments were performed outside the range of validity of (3).

Our numerical procedure is based on a vortex dynamics algorithm that has already proved to be highly accurate and efficient in earlier investigations.[18,19] In Sec. II we will give a brief description of the numerical technique and explain in detail the modifications undertaken to incorporate three-dimensional effects. In Sec. III, results will be presented for the motion of bubbles of two different sizes. We will demonstrate that without three-dimensional effects we reproduce Tanveer's main branch results with a high degree of accuracy, while we do not obtain any steady-state bubble shapes corresponding to the extraordinary branch or the Romero–Vanden-Broeck branches. By taking the leading-order, three-dimensional effects into account, we observe significant changes from the purely two-dimensional results as far as the velocity and shape of the bubbles are concerned. In Sec. IV, we will discuss these results in comparison to the experimental observations.

II. NUMERICAL TECHNIQUE

We aim at simulating the motion of an immiscible bubble of negligible viscosity in a Hele–Shaw cell filled with fluid of viscosity μ. The viscous phase is injected into the cell with average velocity u_0 and thus drives the bubble. Both phases are considered incompressible and give rise to an interfacial tension σ. The balance of pressure and viscous forces, as expressed by the Hele–Shaw equations for a single phase, has to be supplemented by the pressure jump across the interface. The above-mentioned perturbation analysis results, obtained by investigating the flow near the interface in detail, allow us to modify the two-dimensional equations in order to include the leading-order, three-dimensional effects on the pressure jump.

When scaling the momentum equation in the usual way and parametrizing the interface in terms of the arclength s

(e.g., Meiburg and Homsy[19]), we obtain, as dimensionless equations for velocity and pressure,

$$\nabla \cdot \mathbf{u} = 0 , \tag{5}$$

$$\nabla p = -\mu \mathbf{u} - \mathbf{n}\delta(\mathbf{x}-\mathbf{x}_t)\frac{\sigma b^2}{12\mu u_0 L^2} \times\left(\frac{2}{\epsilon}\left[1+\beta\,\mathrm{Ca}_n(s)^{2/3}\right]+\frac{\pi}{4R(s)}\right), \tag{6}$$

where x_t denotes the position of the interface. As pointed out by one referee, this scaled version of the momentum equation provides mathematical justification for neglecting the leakage through the thin film. While this effect is still $O(\mathrm{Ca}^{2/3})$, the pressure jump modification is $O([\epsilon/\mathrm{Ca}]\mathrm{Ca}^{2/3})$. Since we had already assumed that $\epsilon/\mathrm{Ca}^{2/3} \gg 1$, $\epsilon/\mathrm{Ca} \gg 1$ is automatically satisfied, so that the leakage effect can be neglected, compared to the pressure jump modification. By taking the curl of Eq. (6) and introducing the vorticity ω and streamfunction ψ in the usual way, we obtain[19]

$$\mu\omega = \nabla\mu\cdot\nabla\psi - \frac{1}{\mathrm{Ca}}\frac{b^2}{12L^2}\delta(\mathbf{x}-\mathbf{x}_t(s)) \times\frac{\partial}{\partial s}\left(\frac{2}{\epsilon}\beta\,\mathrm{Ca}_n(s)^{2/3}+\frac{\pi}{4R(s)}\right). \tag{7}$$

Knowing the vorticity distribution we can reconstruct the velocity field using the Biot–Savart law,

$$\mathbf{u}(\mathbf{x},t) = -\frac{1}{2\pi}\int\frac{(\mathbf{x}-\mathbf{x}')\times\mathbf{e}_z\omega(\mathbf{x},t)}{|\mathbf{x}-\mathbf{x}'|^2}\,d\mathbf{x}' + \mathbf{u}_{\mathrm{pot}}(\mathbf{x},t), \tag{8}$$

where $u_{\mathrm{pot}}(x,t)$ is the potential part of the velocity field.

The momentum equation in its vorticity form (7) presents the key to the numerical simulation, since it states that the flow field contains vorticity only at locations where the mobility varies and where surface tension acts. For an immiscible flow in which the two phases are separated by a sharp interface, the flow field therefore becomes irrotational, except for the interface itself, which now corresponds to a vortex sheet of strength $\gamma(s)$. Furthermore, Eq. (7) has the advantage of being an algebraic equation, indicating that local information about the flow suffices for the determination of the value of the vorticity. We obtain from (7),

$$\gamma(s) = 2\mathbf{u}\mathbf{t} - \frac{2}{\mathrm{Ca}}\frac{\epsilon^2}{L^2}\delta(\mathbf{x}-\mathbf{x}_t(s)) \times\frac{\partial}{\partial s}\left(\frac{2}{\epsilon}\beta\,\mathrm{Ca}_n(s)^{2/3}+\frac{\pi}{4R(s)}\right). \tag{9}$$

The first term on the right-hand side describes the circulation produced as a result of the mobility jump across the interface. In the absence of surface tension and side walls, it would lead to a circular bubble propagating at twice the velocity of the viscous fluid. In a Hele–Shaw flow of finite width, the additional circulation resulting from the periodic images of the bubble modifies its circular shape and leads to the solutions described by Taylor and Saffman. The remaining terms on the right-hand side account for the influence of surface tension. The third term has the effect of smoothing out variations in the radius of curvature and it modifies the Taylor–Saffman solution toward more circular bubble shapes. The second term represents the additional circulation resulting from the change in the pressure jump as a result of the thin film; its effect on the bubble will be investigated in this paper.

The computational procedure is similar to the one used by Meiburg and Homsy[19] in an earlier investigation of purely two-dimensional viscous fingering, so that we limit ourselves to a brief description of the main features here. The technique is based on Eqs. (8) and (9) and tracks the vortex sheet at the interface in a purely Lagrangian scheme. For the simulation of small bubbles in infinitely wide cells (no wall influence), the integration of the Biot–Savart law has to be carried out only over the interface of this one bubble. For finite ratios of bubble size to cell width, on the other hand, we include the periodic images of the bubble in the y direction. For bubbles symmetric with respect to $y = 0$, which we will deal with exclusively, this corresponds exactly to the condition of no mass flux through the lateral boundaries (Fig. 1).

The vortex sheet is discretized into n small circular arcs, with a marker point denoting the position of each arc. The distribution of the vortex sheet strength along arc i is assumed to be of sinusoidal form. In this way, we can evaluate the associated velocity field by integrating the Biot–Savart law analytically. This form of discretization provides a very smooth and accurate representation of the vortex sheet, as test calculations have demonstrated.[18,19]

As initial bubble shape we use either a circle or an ellipse, since these simple shapes allow us to easily fix the bubble size. After the initial interface shape is set, the calculation proceeds in discrete time steps Δt of size 0.001, based on a fourth-order Runge–Kutta scheme for advancing the marker points. At every time step a new set of circular arcs is fitted through the marker points, and the vortex sheet strength is subsequently updated in an iterative manner. After a fixed number of time steps, 20 for the calculations presented here, the marker points are redistributed and new ones may be added to avoid deteriorating resolution as a result of local interface stretching and shrinking. Both the local capillary number and the local curvature are used to determine the spacing Δs of the marker points along the interface, in the way described in Meiburg and Homsy.[18]

In summary, we apply a numerical procedure, which achieves high spatial accuracy, by discretizing the interface into circular arcs. At the same time it minimizes the effect of

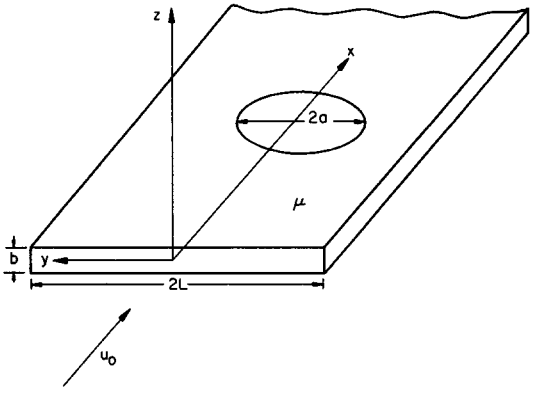

FIG. 1. The principle sketch.

setting a numerical length scale by representing the vorticity sheet along the interface in the form of a continuous distribution. The method is of fourth order in time and partly compensates the $O(N^2)$ operation count associated with the direct interaction algorithm by using a locally refined discretization. All calculations were carried out on the CRAY X-MP of the San Diego Supercomputer Center.

III. RESULTS

Tanveer,[4,5] in his two-dimensional analysis, showed that once a value for the surface tension is set, a bubble of specified area in a Hele–Shaw cell of given size can move only at isolated values of the velocity. He proceeded to determine these values as well as the corresponding bubble shapes. In the following, we will demonstrate the accuracy and convergence of our numerical procedure by reproducing Tanveer's bubble shape. We will subsequently show how varying the capillary number in the simulation will affect the bubble shape as well as its propagation velocity. Of course we will employ the factor of 1, used by Tanveer in the pressure jump condition, instead of $\pi/4$. As a test case we select the bubble corresponding to Tanveer's main branch solution for the parameter values in his notation of $\epsilon = 1.0$, $\alpha = 0.81$, $J = 0.941\,718$, $U = 1.6101$, and $x_B - x_A = 1.0999$. The value of Ca is related to Tanveer's parameters ϵ, α, and U by $\mathrm{Ca} = \pi^2 U b^2/(48 a^2 \epsilon \alpha^2)$. Hence, in a typical experimental apparatus with $\epsilon = 130^{-1}$, such as the one used by Kopf-Sill and Homsy, the present parameters correspond to a value of $\mathrm{Ca} = 2.99 \times 10^{-5}$. While both ϵ and Ca can be considered small, $\epsilon^{-1}\,\mathrm{Ca}^{2/3} = 0.125$. As a result, one would have to be careful about attempting a quantitative comparison between experiments and numerical simulations for these parameter values.

We start our calculation with a circular bubble of area $0.941\,718 L^2$, so the ratio of bubble radius to cell half-width is $a/L = 0.5475$. The bubble subsequently evolves toward a steady state, whose values for bubble length and bubble velocity are given in Fig. 2 as functions of the number of circular arcs used to discretize the bubble contour. The steady state was considered to be reached when the bubble velocity changed by less than 0.1% over a time interval of 5. Figure 2(a) indicates that the bubble velocity is reproduced to within less than 0.5% by discretizing the bubble contour into 15 circular arcs. This demonstrates the high accuracy of our method, even with relatively few computational elements. Discretization into 31 arcs results in an error of about 0.1%. The numerical values for the bubble length are similarly accurate, as shown in Fig. 2(b). We do not observe any signs of instability of this purely two-dimensional solution, even though the calculations were carried out over long times during which the bubble traveled a distance equal to 15 times its rest diameter. From a previous investigation of viscous fingering,[19] we know that instabilities can evolve slowly in an oscillatory fashion. However, we did not discover any signs of such oscillations in the present calculations, which is consistent with Tanveer's result that the main branch represents stable solutions. On the other hand, we were unable to obtain steady solutions corresponding to the extraordinary branch or the first Romero–Vanden-Broeck branch, even when we started our simulation with an elliptic bubble close to the exact solution. These bubbles would invariably evolve toward the shapes given by the main branch, which again is consistent with Tanveer's result of the instability of both the Romero–Vanden-Broeck and the extraordinary solutions.

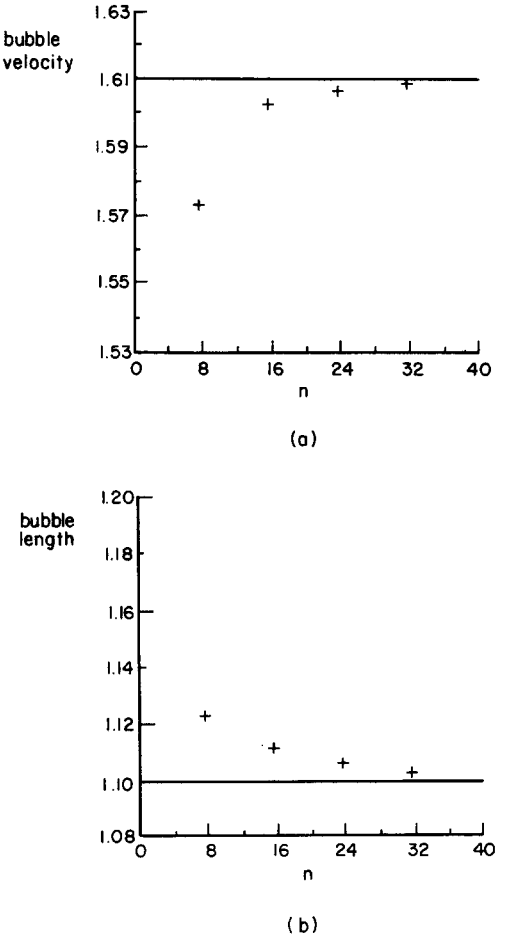

FIG. 2. Convergence of the numerically obtained steady-state bubble data toward Tanveer's main branch results, as a function of number of circular arcs used to discretize the bubble shape: (a) bubble velocity, (b) bubble length.

In Fig. 3 we show the variation of the bubble velocity and bubble length as Ca is varied while ϵ is held constant at the value of 130^{-1}. We can see how the bubble shape becomes more and more circular as the capillary number decreases, i.e., as surface tension forces gain relative importance. Simultaneously, the propagation velocity decreases and then reaches a plateau as the bubble shape does not undergo any further changes. The presence of this plateau for the bubble velocity can be understood from Eq. (9), in terms of the circulation produced by the last term on the right-hand side. This term has the effect of generating circulation as a consequence of variations in $R(s)$, with the result of smoothing out these variations, and at the same time affecting the bubble velocity. For relatively large values of Ca, surface tension can only generate enough circulation to slightly reduce variations in $R(s)$. Consequently, decreasing Ca will lead to further changes in the bubble shape and velocity. However, once an almost perfectly circular bubble shape is reached, there are only small $R(s)$ variations left that add-

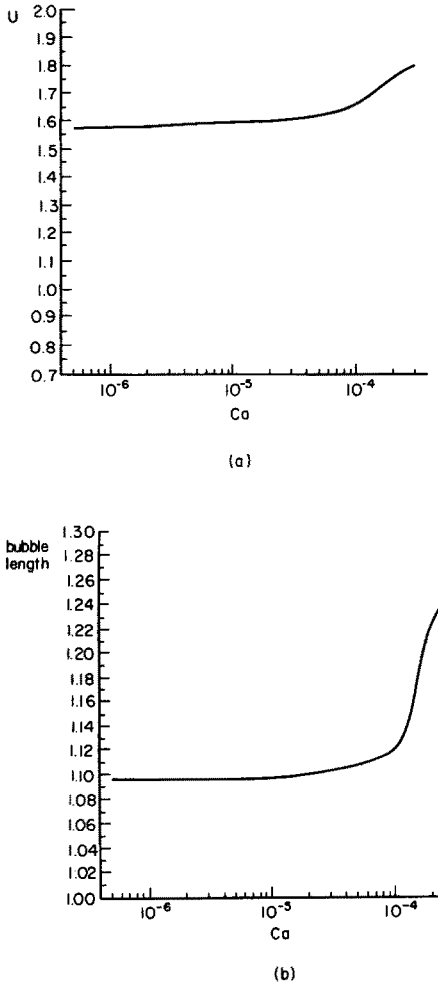

FIG. 3. The steady-state properties of a bubble with $a/L = 0.5475$; only two-dimensional effects are taken into account: (a) bubble velocity, (b) bubble length. As Ca decreases, the elongated bubble monotonically approaches a circular shape, while its velocity reaches a plateau. The value of Ca given is for an aspect ratio $L/b = 130$.

ed surface tension could use to generate additional circulation. As a result, lowering Ca further will not affect the bubble velocity significantly. In other words, as Ca decreases, the circulation distribution asymptotically approaches that of the circular bubble.

As a next step, we consider a bubble of the same size and surface tension, but now we include three-dimensional effects corresponding to an aspect ratio $L/b = 130$, i.e., the value used by Kopf-Sill and Homsy in their experimental investigation. Again we obtain a steady-state bubble, which is depicted in Fig. 4, together with the two-dimensional solution. By comparison with the two-dimensional results, we see that the inclusion of the three-dimensional effects renders the bubble about 2% shorter and wider, and it reduces the propagation velocity by about 12.5% to 1.410. The bubble moved about 8× its rest diameter during our calculation without exhibiting any signs of instability, thus indicating that the inclusion of three-dimensional effects corresponding to an aspect ratio of 130 does not change the bubble's stability characteristics significantly.

The deformation of the two-dimensional bubble and the

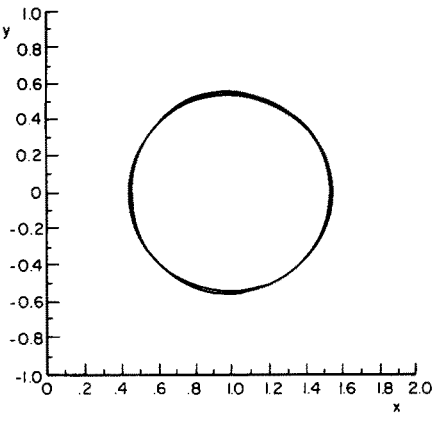

FIG. 4. Steady-state shapes for a bubble of $a/L = 0.5475$. The more elongated shape represents the two-dimensional solution and corresponds to the main branch solution described by Tanveer. The flattened shape takes the leading-order, three-dimensional effects for an aspect ratio $L/b = 130$ into account; i.e., for the value used by Kopf-Sill and Homsy.

decrease in the propagation velocity caused by the three-dimensional effects can be understood in terms of the additional circulation generated along the interface, as a result of the modification in the pressure jump. Figure 5 shows the vortex sheet strength corresponding to the two-dimensional solution as a function of the arclength s, starting from the tip of the bubble and proceeding in the clockwise direction. Along with the two-dimensional calculation the additional vortex sheet strength corresponding to the three-dimensional effects was calculated, without taking its effect on the bubble dynamics into account; the result is also shown in Fig. 5. Thus we can recognize how the three-dimensional effects would deform the bubble if they were allowed to do so. Figure 6 depicts the two-dimensional bubble along with the sign of the three-dimensional circulation along the interface. It is clearly recognizable that the three-dimensional circulation has the effect of slowing down the bubble. The sign of the three-dimensional circulation along the various regions of the interface can also be easily inferred from Eq. (9). As we proceed from the tip along the interface in the clockwise direction, the normal velocity decreases, so $-\beta\,\partial\,\mathrm{Ca}_n/\partial s$ is

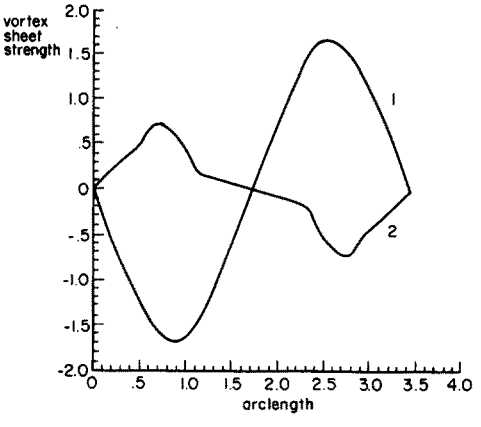

FIG. 5. Vortex sheet strength γ as a function of the arclength s, where s is taken in the clockwise direction from the tip of the bubble. Here 1 is the purely two-dimensional solution and 2 is the leading-order, three-dimensional effect.

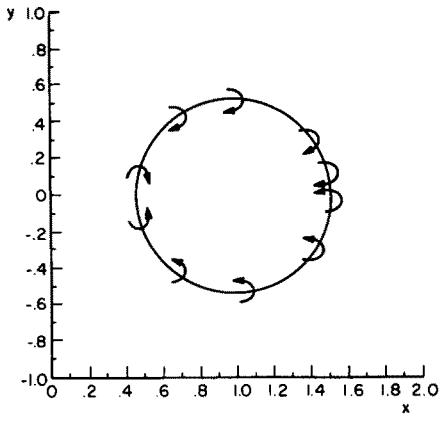

FIG. 6. A sketch of the vortex sheet strength generated by the leading-order, three-dimensional effects. It is obvious that the three-dimensional effects tend to shorten and widen the bubble. At the same time, they induce a negative (upstream) velocity both at the front and at the end of the bubble, thereby slowing it down.

positive. As we approach the rear end, the normal velocity increases again, so that, because of the sign change in β, the resulting circulation remains positive. Since the above is qualitatively true for all nearly circular bubbles, we expect the thin film component of the pressure jump to always slow the bubble down. If the underlying two-dimensional solution remains the same, Eq. (9) states that for $\mathrm{Ca} \approx \mathrm{Ca}_n$ the effect of the thin film should vary approximately with $\epsilon/\mathrm{Ca}^{1/3}$. This is confirmed by Fig. 7, which shows that even as an almost circular bubble shape is reached, the bubble velocity does not approach an asymptotic value as Ca is decreased. Hence the plateau that we had observed for the two-dimensional solution is no longer present.

Whether the bubble flattens or elongates will depend to a large extent on the local circulation distribution around the tip and the tail of the bubble; i.e., it will depend on whether the three-dimensional effects will be more pronounced at the tip or the tail. For a steady, almost circular bubble, $\partial\, \mathrm{Ca}_n (s)^{2/3}/\partial s$ will have approximately the same magnitude close to the tip and close to the tail. However, since the magnitude of β for a receding meniscus is less than one-third of the value for an advancing meniscus, the three-dimensional effects close to the tip will be larger than those close to the tail. As a result, we expect the tip to be decelerated more efficiently by the thin film effects than the tail, so that the bubble will flatten, as seen in Fig. 4.

As a next step, we investigate the properties of the bubble for approximately the same Ca range but for values of ϵ of 70^{-1} and 30^{-1}. Figure 7 shows that the bubble velocity decreases as ϵ increases, while its shape becomes a near circle already at higher values of Ca. Both of these observations are consistent with Eq. (9), which states that for the same underlying two-dimensional problem, i.e., for the same value of ϵ^2/Ca, and for $\mathrm{Ca} \approx \mathrm{Ca}_n$, the slowing effect should vary as $\epsilon/\mathrm{Ca}^{1/3}$. For example, a bubble corresponding to $\mathrm{Ca} = 10^{-6}$ and $\epsilon = 130^{-1}$ gives rise to the same two-dimensional problem as one for $\mathrm{Ca} = 1.88 \times 10^{-5}$ and $\epsilon = 30^{-1}$. According to Eq. (9), however, the second bubble should experience approximately $1.6\times$ as much of a slowdown as the first one, which is confirmed by Fig. 7. For small capillary numbers we observe propagation velocities less than unity, i.e., less than the average velocity of the viscous phase. Figure 8 shows that both the two-dimensional and three-dimensional bubbles approach a circular shape as the capillary number becomes very low. However, while the length of the two-dimensional bubble decreases in a monotonic fashion, the inclusion of three-dimensional effects results in a different behavior: As Ca decreases, the bubble length reaches a minimum before it increases again to the value corresponding to a circle. In other words, while the two-dimensional bubble assumes only slightly elongated shapes, the inclusion of three-dimensional effects leads the bubble to evolve from a slightly elongated shape to a slightly flattened one before it becomes a near circle. The three-dimensional effects, resulting in the slowdown and widening of the bubble, apparently are strong enough in some intermediate capillary number range to cause the bubble to flatten beyond the circular state. As Ca is

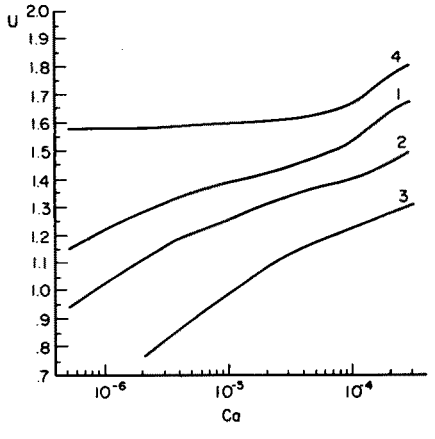

FIG. 7. Propagation velocities for a bubble of $a/L = 0.5475$ when three-dimensional effects are taken into account. The purely two-dimensional data are given for comparison. Here 1: aspect ratio $\epsilon = 1/130$; 2: aspect ratio $\epsilon = 1/70$; 3: aspect ratio $\epsilon = 1/30$; and 4: two-dimensional data. Notice the resulting slowdown of the bubble as ϵ increases. When taking the leading-order, three-dimensional effects into account, we no longer observe a plateau for the propagation velocity.

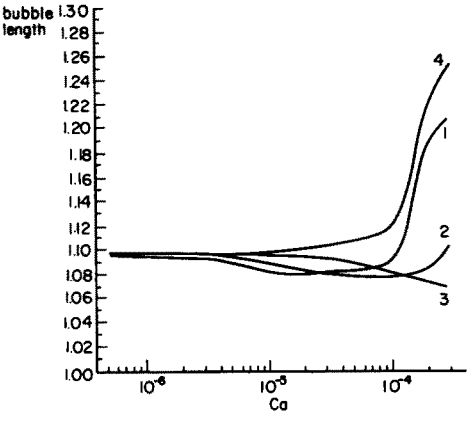

FIG. 8. The bubble lengths for the same parameters as Fig. 7. While the two-dimensional bubble length decreases monotonically with Ca, the three-dimensional effects give rise to a minimum bubble length corresponding to a flattened bubble shape in an intermediate Ca range. The minimum occurs at higher values of Ca as ϵ increases. For small values of Ca, all bubbles approach circular shapes.

lowered further, however, the two-dimensional circulation tends to dominate the flow and causes the bubble to approach a circular shape. The minimum in the bubble length becomes more pronounced as ϵ increases.

We now proceed to simulate a much smaller bubble. We select our parameters according to Tanveer's main branch solution with, in his notation, $\epsilon = 0.2$, $\alpha = 0.2$, $J = 0.050\,948$, $U = 1.976\,76$, and $x_B - x_A = 0.254\,84$. The ratio of bubble radius to cell half-width now is 0.127, i.e., we consider a bubble radius about 4 times smaller than before. As before, we carry out two-dimensional simulations (the capillary number is given for $\epsilon = 130^{-1}$) as well as three-dimensional ones, corresponding to aspect ratios of 130, 100, and 70. Figure 9 shows the variation of the bubble propagation velocity and the bubble length with Ca for these cases. While the two-dimensional simulations again indicate the presence of a plateau for small Ca, the simulations, including three-dimensional effects, show that the slowdown effect is much more pronounced for this smaller size bubble. Furthermore, we notice that for small Ca the bubble velocity varies linearly with log(Ca), the slope being the same for all three aspect ratios investigated. Again we observe bubble propagation velocities smaller than the average velocity of the viscous phase, however, at this time already at higher capillary numbers. Equation (9) presents the key to understanding this behavior: For two steady bubbles of different sizes but similar shapes and propagation velocities, there will be a different distribution of $\partial\beta\,\mathrm{Ca}_n(s)^{2/3}/\partial s$, since for the smaller bubble the variation from $\beta\,\mathrm{Ca}_n$ at the leading meniscus to $\beta\,\mathrm{Ca}_n$ at the trailing meniscus has to occur over a smaller amount of arclength. However, the integral over the circulation distribution, corresponding to the three-dimensional effects from the tip to the tail, will be the same for the two bubbles. Hence in the case of the smaller bubble the same amount of three-dimensional circulation acts to slow the bubble down, but over a smaller distance on average. As a result, the slowing-down effect is more pronounced for the smaller bubble. Figure 10 shows a behavior of the bubble length similar to the one observed for the previous case. While the length of the two-dimensional bubble decreases monotonically to that of a circle, the three-dimensional bubbles exhibit a minimum length for some intermediate value of Ca. For the same aspect ratio, the smaller bubble reaches its minimum length at higher values of Ca than the previously analyzed larger bubble.

As explained above, the existence of a minimum bubble length can be understood as the result of the competition between the two-dimensional and three-dimensional effects. While the two-dimensional forces favor an elongated bubble for higher Ca and a near circle for lower values of Ca, the three-dimensional effects always try to flatten the bubble, even beyond the stage of a circle. It is then natural to ask whether there are parameter ranges for Ca and ϵ in which the three-dimensional forces are able to flatten the advancing meniscus to such a degree that the two-dimensional forces can no longer maintain positive curvature everywhere, with the result of an instability similar to the tip-splitting instability of a viscous finger. We did indeed observe such an instability for the present bubble size at $\mathrm{Ca} = 10^{-2}$ and $\epsilon = 130^{-1}$. Figure 11 shows the evolution of the instability at various times in a moving reference frame. Starting from a circular shape, the bubble tip flattens until it reaches negative curvature and bulges in, thus assuming a shape similar to the "Tanveer" bubbles observed by Kopf-Sill and Homsy. However, this instability did not lead to a new steady state in our simulations; instead it grew until the calculation failed to converge. Furthermore, we have to point out that although Ca and ϵ are both small numbers, $\epsilon^{-1}\,\mathrm{Ca}^{2/3} \approx 6$, so that we are outside of the range of validity of the perturbation expansion on which we based our numerical simulation. In addition, the condition of equal bubble curvature at the front and rear stagnation points, for which numerical values for β had been derived, is no longer satisfied. Hence we cannot expect quantitative agreement with experimental observations. Nonetheless it is of interest to observe in which direction the three-dimensional effects tend to shift the stable main branch solution.

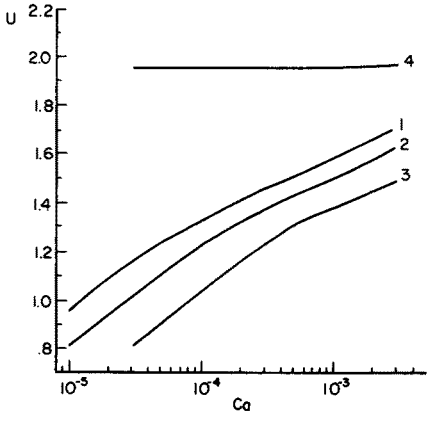

FIG. 9. Propagation velocities for a bubble of $a/L = 0.127$ when three-dimensional effects are taken into account. The purely two-dimensional data are given for comparison. Here 1: aspect ratio $\epsilon = 1/130$; 2: aspect ratio $\epsilon = 1/100$; 3: aspect ratio $\epsilon = 1/70$; and 4: two-dimensional data. The slowdown of the bubble as ϵ increases is more pronounced for this smaller bubble velocity. For small Ca, the bubble velocity depends linearly on log(Ca), the slope being the same for all three aspect ratios.

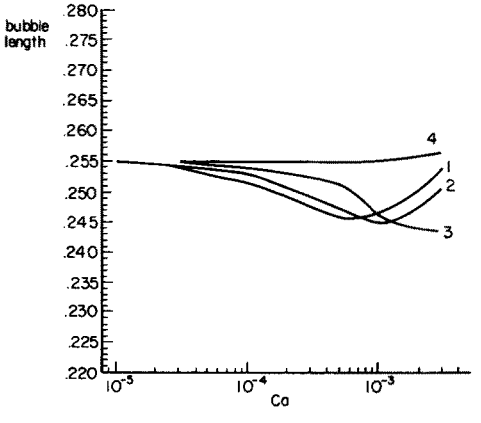

FIG. 10. The bubble lengths for the same parameters as Fig. 9. Again we observe a minimum in the bubble length if three-dimensional effects are taken into account. However, for this smaller bubble, the minimum occurs at higher values of Ca. As before, all bubbles approach circular shapes or small values of Ca.

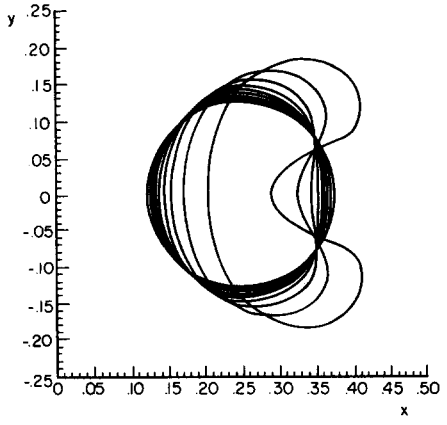

FIG. 11. For $a/L = 0.127$, $\epsilon = 130^{-1}$, and $\mathrm{Ca} = 10^{-2}$ the bubble develops a splitting instability similar to the tip splitting of viscous fingers. Shown in a moving reference frame are the bubble shapes at times 0.02, 1.0, 1.26, 1.5, 1.76, 2.0, 2.26, 2.5, and 2.76. While the above parameter values lie outside the range of validity of the perturbation expansion, we can conclude that the three-dimensional effects promote the evolution of a tip-splitting instability. This provides a possible explanation for the emergence of experimentally observed "Tanveer" bubbles.

As discussed above, the additional circulation induced by the three-dimensional effects leads to a slowdown of the bubble tip and the bubble tail, which is compatible with our observation that it can lead to a tip-splitting instability. It is then logical to ask whether, in a similar way, the three-dimensional effects can lead to a slowdown of the bubble's rear meniscus and thus result in the formation of short or long tails, as observed by Kopf-Sill and Homsy. We examined a few bubble shapes concerning this possibility, but even attempts to trigger the instability by artificially slowing down the rear meniscus for a short time interval did not yield any such bubble shapes.

IV. DISCUSSION

We have presented numerical simulations for the propagation of bubbles in Hele–Shaw cells with and without three-dimensional effects. For the purely two-dimensional case our results converge to Tanveer's main branch solution with high accuracy. In agreement with his solutions, our simulations yield only elongated bubbles with propagation velocities larger than the average velocity of the viscous phase. We never observed the evolution of a steady-state two-dimensional bubble corresponding to the extraordinary branch or to one of the Romero–Vanden-Broeck branches, even if the initial conditions for the simulations were close to these steady-state solutions. Thus our time-dependent numerical simulations are consistent with Tanveer's results concerning the stability of steady-state solutions.

Subsequently we modified our numerical algorithm to include the leading-order effects of the thin film on the pressure jump across the interface. For the two bubble sizes investigated, the additional circulation created by the leading-order, three-dimensional correction leads to a widening and shortening of the bubble as well as to a reduction of its propagation velocity, which can immediately be understood in terms of the dynamics of the additional circulation. The slowdown is most pronounced for the smaller bubble. While the purely two-dimensional simulations had shown the existence of a plateau for the propagation velocity as Ca reached very small values, such a plateau was not observed when we included three-dimensional effects. Instead, the bubble velocity kept decreasing with the capillary number. In particular, we observed propagation velocities lower than the average fluid velocity. While the velocity does not level off in the parameter ranges investigated here, it is expected to reach a plateau as Ca becomes very small.

The limited range of validity of the perturbation expansion on which our simulations are based does not allow us to make quantitative comparisons with the experiments of Kopf-Sill and Homsy. However, we note that in all but one of their series of experiments they observe a general trend of decreasing bubble velocities as Ca is reduced. Furthermore, their experiments do not indicate a lower bound for the velocity as Ca decreases, also in qualitative agreement with out simulations. Our numerically obtained bubble shapes agree qualitatively with the experiments of Kopf-Sill and Homsy only insofar as both show near circles for low Ca (with the exception of their series 5) and elongated bubbles for higher Ca. If flattened bubbles were seen in the experiments, they always appeared in between the near circles and the elongated bubbles, in agreement with our simulations.

The simulations allowed us to explain the existence of flattened bubbles as a result of the competition between two- and three-dimensional effects. This leads to the question of whether there are parameter ranges for which the three-dimensional effects would be strong enough to overcome the two-dimensional forces and cause a splitting instability. We did observe such a splitting instability, however, only for parameter values outside the range of validity of the perturbation expansion. We conclude that the leading-order, three-dimensional effects promote the tip-splitting instability without being large enough to explain the experimental observation of "Tanveer" bubbles.

In this context it is interesting to note the following fact: for constant surface tension and bubble size, the inclusion of three-dimensional effects results in a shorter, wider, and slower bubble. That, on the other hand, is exactly how the Romero–Vanden-Broeck branch differs from the main branch; it also describes shorter, wider, and slower bubbles. As a result, it appears possible that by including three-dimensional effects, we cause the main branch solution to become unstable with respect to the tip instability mode of the Romero–Vanden-Broeck branch found by Tanveer and Saffman.[3] We did not observe any steady-state solutions with negative tip curvature, and hence we assume that three-dimensional effects, other than the leading-order ones on the pressure jump, must be responsible for the stabilization of the experimentally observed bubbles of this nature.

In our numerical simulations we never observed any instabilities that would resemble the short tail and the long tail bubbles found by Kopf-Sill and Homsy. These instability modes affect the bubble tail and appear to be related to the least stable modes found by Tanveer and Saffman for bubbles corresponding to the main branch solution. Comparison of the experiments and stability theory suggests that the three-dimensional effects destabilize the main branch solu-

tion and cause the least stable mode to become unstable. This is compatible with our calculations, which show that the leading-order, three-dimensional effects induce an upstream velocity at the rear meniscus of the bubble. In a way similar to the tip instability discussed above, once this instability has developed a certain finite amplitude, the bubble becomes stabilized and reaches a steady state. Most likely, an analysis of the full three-dimensional flow will be necessary to explain this nonlinear stability. On the basis of our numerical simulations we cannot fully explain the destabilization of the main branch solutions with respect to the bubble tail instability.

Hence, taken together, experiments, stability theory, and numerical simulations indicate that three-dimensional effects can cause the main branch solution to become unstable in at least two different ways: (i) they can shift the main branch solution toward the Romero–Vanden-Broeck branch and thus result in instability with respect to the symmetric and antisymmetric tip instability modes of this branch, and (ii) they can cause the least stable mode of the main branch to become unstable and result in a bubble tail instability. For both the symmetric tip instability and the tail instability a new stable bubble shape is reached after the instability has achieved a certain finite amplitude. However, so far there are no indications for stable antisymmetric bubbles. As a result, it appears that there are at least three different parameter regions in which different steady state shapes can exist for a bubble of a certain size. In this way, it would be possible to explain the dramatic transitions between different classes of bubble shapes recorded by Kopf-Sill and Homsy. Overlap of these different regions of stability could account for the hysteresis effects they observe. It is obvious that the present numerical simulations can at best provide some qualitative information, since they only include the leading-order, three-dimensional effects. It is expected that fully three-dimensional simulations will be able to contribute greatly to further understanding.

ACKNOWLEDGMENTS

The author would like to thank Professor G. M. Homsy for his continued interest in this work as well as for several helpful discussions and comments.

This work was supported by DARPA under URI contract N00014-86-K0754 as well as by the San Diego Supercomputer Center, which provided the computing time.

[1]G. M. Homsy, Annu. Rev. Fluid Mech. **19**, 271 (1987).
[2]P. G. Saffman, J. Fluid Mech. **173**, 73 (1986).
[3]S. Tanveer and P. G. Saffman, Phys. Fluids **30**, 2624 (1987).
[4]S. Tanveer, Phys. Fluids **29**, 3537 (1986).
[5]S. Tanveer, Phys. Fluids **30**, 651 (1987).
[6]A. R. Kopf-Sill and G. M. Homsy, Phys. Fluids **31**, 18 (1988).
[7]F. P. Bretherton, J. Fluid Mech. **10**, 166 (1961).
[8]C.-W. Park and G. M. Homsy, J. Fluid Mech. **139**, 291 (1984).
[9]D. A. Reinelt, J. Fluid Mech. **183**, 219 (1987).
[10]A. R. Kopf-Sill and G. M. Homsy (private communication).
[11]G. I. Taylor and P. G. Saffman, Q. J. Mech. Appl. Math **12**, 265 (1959).
[12]J. McLean and P. G. Saffman, J. Fluid Mech. **102**, 455 (1981).
[13]L. Romero, Ph. D. dissertation, California Institute of Technology, 1982.
[14]J.-M. Vanden-Broeck, Phys. Fluids **26**, 2033 (1983).
[15]S. Tanveer (private communication).
[16]A. R. Kopf-Sill and G. M. Homsy, Phys. Fluids **31**, 18 (1988).
[17]T. Maxworthy, J. Fluid Mech. **173**, 95 (1986).
[18]E. Meiburg and G. M. Homsy, *Proceedings of the Symposium on Numerical Simulation in Oil Recovery*, edited by M. Wheeler (Springer, Berlin, 1988).
[19]E. Meiburg and G. M. Homsy, Phys. Fluids **31**, 429 (1988).